ELSEVIER

International Journal of Solids and Structures 41 (2004) 4435–4456

INTERNATIONAL JOURNAL OF SOLIDS and STRUCTURES

www.elsevier.com/locate/ijsolstr

Large plastic deformation of metallic honeycomb: orthotropic rate-independent constitutive model

Dirk Mohr *, Mulalo Doyoyo

Impact and Crashworthiness Laboratory, Massachusetts Institute of Technology, Room 5-222, 77 Massachusetts Avenue, Cambridge, MA 02139, USA

Received 24 October 2003; received in revised form 17 February 2004
Available online 15 April 2004

Abstract

This paper deals with the development of a phenomenological, orthotropic, rate-independent constitutive model of metallic honeycombs guided by earlier experimental investigations. Previous physical and virtual experiments have shown that under large out-of-plane deformation, the cellular microstructure of a honeycomb is progressively folded while the macroscopic normal and shear stress–strain curves exhibit pronounced stress plateaus. Furthermore, it follows from the experimental results that in a monolithic hexagonal honeycomb, the direction of macroscopic plastic flow during crushing under combined out-of-plane loading is coaxial with the direction of the compressive principal stress. Based on these experimental observations, a constitutive model is formulated that describes the out-of-plane mechanical behavior of a metallic honeycomb in the crushing and densification regimes. The model is incorporated into a commercial finite element code and successfully utilized to simulate several biaxial experiments on a hexagonal aluminum honeycomb. A universal procedure to calibrate the model for other types of metallic honeycombs is provided.

Keywords: Honeycomb; Constitutive model; Plasticity; Large deformations; Sandwich structures

1. Introduction

Metallic honeycombs are frequently used as lightweight core materials in sandwich structures. The use of honeycombs is often justified by their high out-of-plane shear moduli at low mass density. Example applications in the area of stiffness-based designs include various structural elements of modern aircrafts such as cabin floor panels, wing structures or jet engine housings. In automotive engineering, sandwich structures with honeycomb cores are being proposed as an alternative to stiffened sheet metal assemblies. Such applications typically require the forming of flat sandwich sheets into three-dimensionally shaped shell structures, which involves large plastic deformation of the honeycomb core. Large plastic deformations of honeycombs also characterize the mechanical response during accidental impact loading of sandwich

* Corresponding author. Tel.: +1-617-253-0989; fax: +1-617-253-8125.
E-mail address: mohr@mit.edu (D. Mohr).

0020-7683/$ - see front matter © 2004 Elsevier Ltd. All rights reserved.
doi:10.1016/j.ijsolstr.2004.02.062

structures. For example, a pedestrian hitting the sandwich hood of a car, birds colliding with aircrafts, or shock waves reaching the outer hull of ships.

A characteristic feature of a honeycomb microstructure is its orthotropy. The cellular microstructure of a honeycomb comprises a network of joined, parallel, thin-walled tubes with a given cross-sectional profile. For a hexagonal honeycomb, the initial orthotropy directions may be denoted as the W-, L-, and T-directions (Fig. 1). The T-direction, also known as the out-of-plane direction, is aligned with the axis of the thin-walled tubes. The additional two directions, the so-called in-plane directions (W and L), denote the ribbon and length directions of the hexagonal cross-section, respectively (Fig. 1). The elastic stiffnesses in the W- and L-directions as well as the stiffness for shear loading in the W–L plane are typically by one to two orders of magnitudes lower than those with respect to the out-of-plane direction (that includes normal loading in the T-direction and shear loading in the T–W and T–L planes). The stress levels during plastic loading may be described in a similar manner. To illustrate, we summarized the characteristic mechanical properties of a commercial hexagonal aluminum honeycomb in Table 1. This honeycomb deforms plastically at a stress of 0.02 MPa when loaded in the W-direction. However, a stress of about 0.9 MPa is required to crush the honeycomb along the T-direction. This observation leads to an essential assumption in the present model. That is, the internal energy variation under in-plane loading is negligibly small as compared to that under out-of-plane loading. In other words, we ignore in-plane loading and focus on the modeling of the out-of-plane behavior. It is worth noting that many previous studies on honeycombs dealt with the in-plane response. Such studies were mainly carried-out in order to gain understanding on the mechanical response of metal foams (e.g. Okumura et al., 2002).

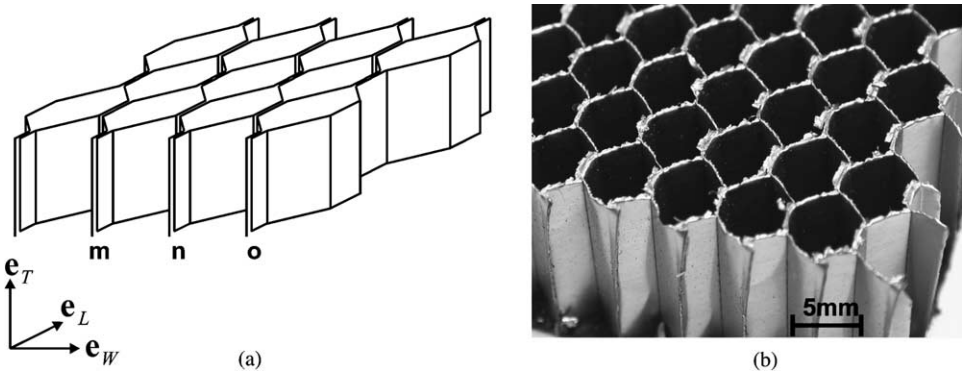

Fig. 1. Microstructural geometry of a hexagonal honeycomb. (a) Schematic with coordinate system: the cell wall labels m, n, o establish the link between the undeformed geometry and the deformed specimen that is shown in Fig. 10; (b) photograph of the 1.8% relative density hexagonal aluminum 5056-H39 honeycomb.

Table 1
Mechanical properties of 1.8% relative density hexagonal aluminum 5056-H39 honeycomb

E_{WW} (MPa)	E_{LL} (MPa)	G_{WL} (MPa)	σ^y_{WW} (MPa)	σ^y_{LL} (MPa)	τ^y_{WL} (MPa)
In-plane properties					
0.11	0.27	0.02	0.02	0.03	0.05
E_{TT} (MPa)	G_{TW} (MPa)	G_{TL} (MPa)	σ^y_{TT} (MPa)	τ^y_{TW} (MPa)	τ^y_{TL} (MPa)
Out-of-plane properties					
1253	156	315	0.93	0.53	n.a.

The out-of-plane behavior of a honeycomb under large deformations has been documented in previous experimental studies (Doyoyo and Mohr, 2003; Mohr and Doyoyo, 2003a–d). The typical mechanical response of a honeycomb under uniaxial compression in the T-direction is shown in Fig. 2. In the elastic regime, the stress–strain curve is initially linear, but becomes non-linear at the later stages due to elastic buckling of the cellular microstructure. When the local stresses in the cell walls exceed the yield threshold, the elastic regime ends and the honeycomb microstructure collapses. This point is characterized by a peak stress that is followed by a short softening regime preceding the crushing regime. In the crushing regime, the cell walls are progressively folded. The folding process is mirrored in the macroscopic stress–strain curve by small fluctuations around a constant stress plateau. The crushing regime persists over a wide range of strains until the entire microstructure is folded and the stress rises as the folded microstructure is densified. A similar response is observed under combinations of compressive and shear loading along the T- and W-directions, respectively (Fig. 3), however at different stress levels (Mohr and Doyoyo, 2004a,b).

It is important to note that deformation localizes within the honeycomb microstructure as compressive loads are applied along the T-direction. For in-plane problems involving microstructural deformation

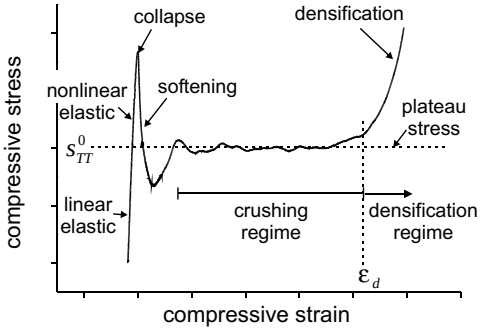

Fig. 2. Characteristic stress–strain curve for metallic honeycomb under uniaxial compression along the T-direction.

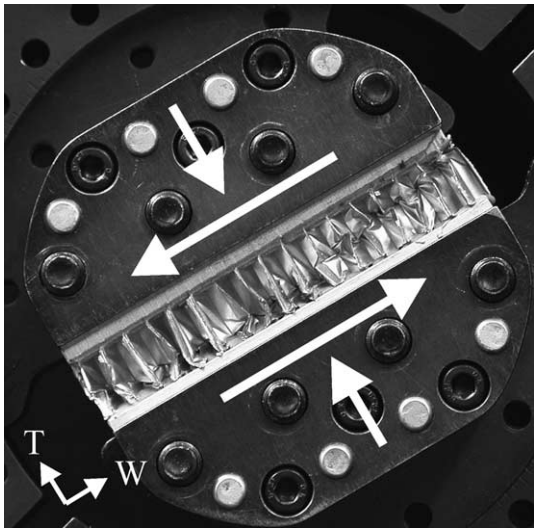

Fig. 3. Localization of deformation in an aluminum honeycomb specimen under combined normal and shear loading in the T–W plane.

mechanisms that result in an unstable macroscopically heterogeneous material, two-scale theories or special homogenization methods may be used to develop the constitutive model for the material (e.g. Triantafyllidis and Maker, 1985; Geymonat et al., 1993, Ohno et al., 2002). With respect to constitutive modeling of the out-of-plane behavior of a honeycomb, three distinct approaches are proposed:

(1) Imperfection-informed constitutive modeling of the propagation of folds in the honeycomb microstructure (Mohr and Doyoyo, 2003b). This approach directly addresses the problem of deformation localization during the out-of-plane crushing of honeycomb.
(2) Microstructure-based modeling of the kinematics of cell wall folding. Analogously to crystal plasticity, this approach assumes that the folding of the honeycomb microstructure is controlled by the deformation-induced fold systems (Mohr and Doyoyo, 2004b).
(3) Phenomenological modeling of the macroscopic, mechanical behavior. The localization of deformation is ignored and the deforming microstructure is considered as being statistically homogeneous at the macroscopic level. This approach is focused on predicting the macroscopic stress and strain fields.

In this paper, we consider the latter approach and develop a phenomenological constitutive model of metallic honeycombs that describes the out-of-plane mechanical behavior in the crushing and densification regimes. Without addressing the issue of localization of deformation, Schreyer et al. (1994) proposed a three-dimensional anisotropic plasticity model for honeycombs. Using the results from uniaxial compression experiments along the T-direction, Schreyer et al. assumed a spherical yield surface in the principal stress space, while the center of the yield surface is shifted in stress space. However, biaxial tests clearly disprove this assumption (Fig. 4). Widely used heuristic constitutive models of honeycombs that are built into commercial finite element codes such as PamCrash (model 41, ESI, 2000) neglect the interaction between shear and normal stresses. They comprise six separate fully-uncoupled one-dimensional constitutive equations for each component of the stress tensor. The experimental results by Mohr and Doyoyo (2004a) reveal that the use of such models may overestimate the plastic work by as much as 100% when the honeycomb is subjected to combined normal and shear loading in the T–W plane (Fig. 4).

Based on previous experimental observations, we develop a phenomenological constitutive model of metallic honeycomb. The central assumptions are (1) the in-plane strains are small, (2) the out-of-plane stresses do not depend on the in-plane strains, (3) the in-plane stresses are negligibly small, and (4) the concept of plateau stresses applies, i.e. the assumption of normal and shear stress plateaus in the crushing

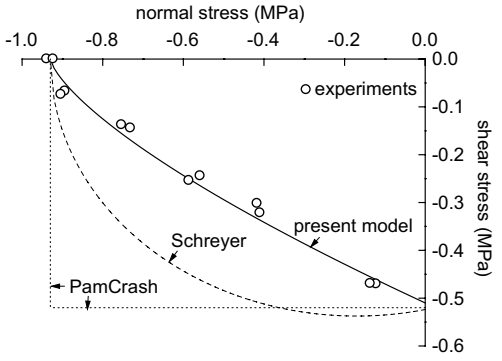

Fig. 4. Comparison of yield surfaces: the dotted rectangle indicates the yield surface in the PamCrash (model 41) and the dashed line shows the elliptic envelope by Schreyer et al. (1994). Each open circle represents an experimental data point as obtained from biaxial tests (Mohr and Doyoyo, 2004a), while the solid line shows the crushing envelope that is assumed by the present model.

regime provides a satisfactory approximation for the complex stress–strain response. The yield surface is conical in the shear–normal stress space, while the direction of plastic flow is governed by the direction of the compressive principal stress. We employ an Euler backward-integration scheme to implement the constitutive model into a finite element program and use it to simulate several uniaxial and multiaxial experiments on hexagonal aluminum honeycomb. The reasonable agreement between the predictions of the model and the experimental results encourages the use of the present model for applications involving large plastic out-of-plane deformation of metallic honeycombs.

2. Phenomenological constitutive model

Our constitutive equations are specifically tailored for metallic honeycombs right from the beginning. In the present formulation, we introduce new definitions of stress and strain in order to establish a clear link between the model assumptions and experimental observations (Mohr and Doyoyo, 2004a,b). Alternatively, the constitutive equations could also be formulated using other stress and strain definitions such as the Cauchy stress tensor along with the rate-of-deformation tensor or the second Piola–Kirchhoff stress tensor along with Lagrangian strains.

Throughout our presentation, we use the notation of modern continuum mechanics (e.g. Gurtin, 1981). Specifically, $\mathbf{a}\cdot\mathbf{b}$ denotes the scalar (inner) product of two vectors $\mathbf{a}$ and $\mathbf{b}$; $\mathbf{a}\otimes\mathbf{b}$ denotes the dyadic (tensor) vector product, that yields a linear transformation defined as $(\mathbf{a}\otimes\mathbf{b})\mathbf{c}=(\mathbf{c}\cdot\mathbf{b})\mathbf{a}$, where $\mathbf{c}$ is a vector of the same dimension as $\mathbf{a}$ and $\mathbf{b}$. Vectors with components $\{1,0,0\}^{\mathrm{T}}$, $\{0,1,0\}^{\mathrm{T}}$, and $\{0,0,1\}^{\mathrm{T}}$ are denoted as $\mathbf{e}_1$, $\mathbf{e}_2$, and $\mathbf{e}_3$, respectively. (Note: the superscript 'T' denotes the transpose of a vector or matrix, whereas the subscript T indicates the coordinate axis T.)

2.1. Material coordinate system

The constitutive model is formulated in material coordinates which is attached to the orthotropy axes of the initial configuration of the honeycomb. Given the unit vectors $(\mathbf{e}^{\mathrm{g}}_W,\mathbf{e}^{\mathrm{g}}_L,\mathbf{e}^{\mathrm{g}}_T)$ of the three initial orthotropy axes in global coordinates (Fig. 1), we can define the coordinate system transformation tensor $\mathbf{B}$ as

$$\mathbf{B}=\mathbf{e}_1\otimes\mathbf{e}^{\mathrm{g}}_W+\mathbf{e}_2\otimes\mathbf{e}^{\mathrm{g}}_L+\mathbf{e}_3\otimes\mathbf{e}^{\mathrm{g}}_T. \tag{1}$$

A vector $\mathbf{a}$ given in global coordinates is then expressed in material coordinates as

$$\mathbf{a}^{\mathrm{g}}\rightarrow\mathbf{a}^{\mathrm{m}}=\mathbf{B}\mathbf{a}^{\mathrm{g}}, \tag{2}$$

where the superscripts 'g' and 'm' refer to the corresponding 'global' and 'material' coordinate systems, respectively. Accordingly, the coordinate system transformation of the deformation gradient tensor $\mathbf{F}$ reads

$$\mathbf{F}^{\mathrm{g}}\rightarrow\mathbf{F}^{\mathrm{m}}=\mathbf{B}\mathbf{F}^{\mathrm{g}}\mathbf{B}^{\mathrm{T}} \tag{3}$$

and analogously, we have the transformation of the Cauchy stress tensor $\mathbf{T}$ from global to material coordinates as

$$\mathbf{T}^{\mathrm{g}}\rightarrow\mathbf{T}^{\mathrm{m}}=\mathbf{B}\mathbf{T}^{\mathrm{g}}\mathbf{B}^{\mathrm{T}}. \tag{4}$$

Conversely, the transformation from material to global coordinates can be obtained as $\mathbf{T}^{\mathrm{m}}\rightarrow\mathbf{T}^{\mathrm{g}}=\mathbf{B}^{\mathrm{T}}\mathbf{T}^{\mathrm{m}}\mathbf{B}$. In what follows, we omit the superscript that indicates the coordinate system. All tensors and vectors are given in material coordinates, i.e. $\mathbf{F}:=\mathbf{F}^{\mathrm{m}}$ and $\mathbf{T}:=\mathbf{T}^{\mathrm{m}}$.

2.2. Kinematics of finite strain

We decompose the deformation gradient into a stretch tensor **U** and a rotation tensor **R**:

$$\mathbf{F} = \mathbf{R}\mathbf{U}. \tag{5}$$

This decomposition is typically performed according to the fundamental rotation theorem, which states that **R** is an orthogonal rotation tensor and **U** is a symmetric positive-definite tensor (e.g. Malvern, 1969). In the present model, we also assume that **R** is an orthogonal rotation tensor, but we use a physical argument for the decomposition of **F**, which yields a non-symmetric stretch tensor **U**. Here, we chose **R** such that it describes the rotation of the *W–L* plane. Thus, the deformation field is described by the stretch tensor **U** that is free from any rigid body rotation of the *W–L* plane. The sketch in Fig. 5 illustrates this decomposition. We define the strain tensor **E** as

$$\mathbf{E} = \mathbf{U} - \mathbf{1}. \tag{6}$$

As a result of this simple form of the strain tensor, individual components correspond to the strains γ_{TW}, γ_{TL} and ε_{TT} (see Fig. 6) that are typically measured in experiments (see Mohr and Doyoyo, 2004a,b):

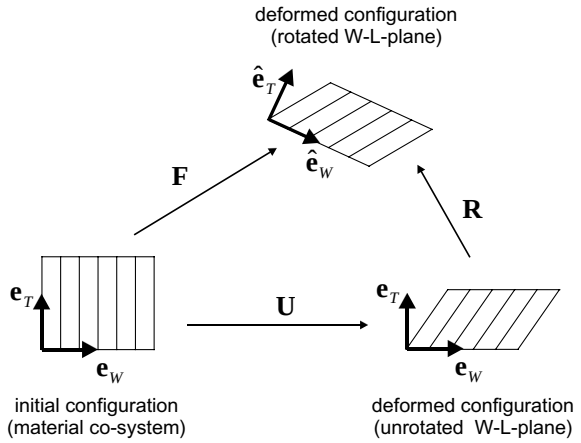

Fig. 5. Kinematics.

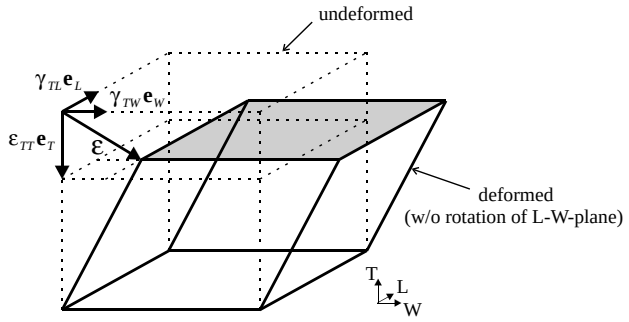

Fig. 6. Homogeneous out-of-plane deformation of a unit cube from the undeformed configuration (- - -) to the deformed configuration (—).

$$E_{13} = \mathbf{E} \cdot (\mathbf{e}_1 \otimes \mathbf{e}_3) = \gamma_{TW}, \tag{7}$$

$$E_{23} = \mathbf{E} \cdot (\mathbf{e}_2 \otimes \mathbf{e}_3) = \gamma_{TL}, \tag{8}$$

$$E_{33} = \mathbf{E} \cdot (\mathbf{e}_3 \otimes \mathbf{e}_3) = \varepsilon_{TT}. \tag{9}$$

Mathematically, we write the rotation $\mathbf{R}$ as

$$\mathbf{R} = \mathbf{e}_1 \otimes \hat{\mathbf{e}}_W + \mathbf{e}_2 \otimes \hat{\mathbf{e}}_L + \mathbf{e}_3 \otimes \hat{\mathbf{e}}_T, \tag{10}$$

where the vector $\hat{\mathbf{e}}_T$ denotes the normal to the W–L plane in the rotated deformed configuration and $\hat{\mathbf{e}}_W$, $\hat{\mathbf{e}}_L$ are the corresponding rotated in-plane directions:

$$\begin{aligned} \hat{\mathbf{e}}_W &= \frac{\mathbf{F}\mathbf{e}_W}{\|\mathbf{F}\mathbf{e}_W\|}, \\ \hat{\mathbf{e}}_L &= \frac{\mathbf{F}\mathbf{e}_L}{\|\mathbf{F}\mathbf{e}_L\|}. \end{aligned} \tag{11}$$

The vectors $\hat{\mathbf{e}}_W$ and $\hat{\mathbf{e}}_L$ are not necessary perpendicular to each other in the deformed configuration, but we demand that the in-plane distortion be small, i.e.

$$\hat{\mathbf{e}}_W \cdot \hat{\mathbf{e}}_L \cong 0. \tag{12}$$

The third unit vector, $\hat{\mathbf{e}}_T$, that is perpendicular to the rotated W–L plane is obtained as

$$\hat{\mathbf{e}}_T = \frac{\hat{\mathbf{e}}_W \times \hat{\mathbf{e}}_L}{\|\hat{\mathbf{e}}_W \times \hat{\mathbf{e}}_L\|}. \tag{13}$$

And finally, in order to ensure the exact orthogonal nature of the base vectors, we recalculate $\hat{\mathbf{e}}_L$ from the cross product of the $\hat{\mathbf{e}}_W$ and $\hat{\mathbf{e}}_T$ vectors:

$$\hat{\mathbf{e}}_L = \hat{\mathbf{e}}_T \times \hat{\mathbf{e}}_W. \tag{14}$$

Thus, the rotation tensor $\mathbf{R}$ is uniquely determined by Eqs. (10), (11), (13) and (14), and we can compute the non-symmetric strain tensor (Eq. (6)) as

$$\mathbf{E} = \mathbf{R}^{\mathrm{T}}\mathbf{F} - \mathbf{1}. \tag{15}$$

2.3. Thermodynamic framework

According to the Clausius–Duhem inequality for an isothermal process, the rate of dissipation, φ, must be positive:

$$\varphi = W - \dot{\psi} \geqslant 0, \tag{16}$$

where W denotes the stress power and $\dot{\psi}$ denotes the time rate of the Helmholtz free energy, both defined per unit initial volume. The stress tensor $\mathbf{T}^*$ which is the work conjugate of the strain tensor $\mathbf{E}$ defined by Eq. (15), can be evaluated from the stress power. The starting point is the expression of the stress power in terms of the Cauchy stress tensor $\mathbf{T}$ and the rate-of-deformation tensor $\mathbf{L} = \dot{\mathbf{F}}\mathbf{F}^{-1}$:

$$\begin{aligned} W &= (\det \mathbf{F})\mathbf{T} \cdot \mathbf{L} = (\det \mathbf{F})\mathbf{T} \cdot \dot{\mathbf{F}}\mathbf{F}^{-1} = (\det \mathbf{U})\mathbf{T} \cdot \dot{\mathbf{R}}\mathbf{R}^{\mathrm{T}} + (\det \mathbf{U})\mathbf{T} \cdot \mathbf{R}\dot{\mathbf{U}}\mathbf{U}^{-1}\mathbf{R}^{\mathrm{T}} \\ &= (\det \mathbf{U})\mathbf{R}^{\mathrm{T}}\mathbf{T}\mathbf{R}\mathbf{U}^{-\mathrm{T}} \cdot \dot{\mathbf{U}} = \mathbf{T}^* \cdot \dot{\mathbf{E}}, \end{aligned} \tag{17}$$

where the work conjugate stress tensor reads

$$\mathbf{T}^* = (\det \mathbf{U})\mathbf{R}^{\mathrm{T}}\mathbf{T}\mathbf{R}\mathbf{U}^{-\mathrm{T}}. \tag{18}$$

The main assumption in this model is the negligence of the work done by the in-plane stresses. Thus, the expression for the stress power reduces to

$$W = \mathbf{T}^* \cdot \dot{\mathbf{E}} \cong T^*_{13}\dot{E}_{13} + T^*_{23}\dot{E}_{23} + T^*_{33}\dot{E}_{33} = \tau_{TW}\dot{\gamma}_{TW} + \tau_{TL}\dot{\gamma}_{TL} + \sigma_{TT}\dot{\varepsilon}_{TT} = \boldsymbol{\sigma} \cdot \dot{\boldsymbol{\varepsilon}}, \tag{19}$$

where we introduced the stress vector,

$$\boldsymbol{\sigma} = \begin{Bmatrix} T^*_{13} \\ T^*_{23} \\ T^*_{33} \end{Bmatrix} = \begin{Bmatrix} \tau_{TW} \\ \tau_{TL} \\ \sigma_{TT} \end{Bmatrix} \tag{20}$$

and the strain vector, $\boldsymbol{\varepsilon}$,

$$\boldsymbol{\varepsilon} = \begin{Bmatrix} E_{TW} \\ E_{TL} \\ E_{TT} \end{Bmatrix} = \begin{Bmatrix} \gamma_{TW} \\ \gamma_{TL} \\ \varepsilon_{TT} \end{Bmatrix}. \tag{21}$$

The constitutive model will describe the relationship between the stress vector $\boldsymbol{\sigma}$ and the strain vector $\boldsymbol{\varepsilon}$ for an arbitrary loading path.

We consider the additive decomposition of the strain vector into its elastic part $\boldsymbol{\varepsilon}^{\mathrm{e}}$ and its plastic part $\boldsymbol{\varepsilon}^{\mathrm{p}}$:

$$\boldsymbol{\varepsilon} = \boldsymbol{\varepsilon}^{\mathrm{e}} + \boldsymbol{\varepsilon}^{\mathrm{p}} \tag{22}$$

and we define the free Helmholtz energy as a function of the elastic strain vector:

$$\psi = \hat{\psi}(\boldsymbol{\varepsilon}^{\mathrm{e}}). \tag{23}$$

Combining Eqs. (16), (19) and (23), we get

$$\varphi = \left(\boldsymbol{\sigma} - \frac{\partial\hat{\psi}}{\partial\boldsymbol{\varepsilon}^{\mathrm{e}}}\right) \cdot \dot{\boldsymbol{\varepsilon}}^{\mathrm{e}} + \boldsymbol{\sigma} \cdot \dot{\boldsymbol{\varepsilon}}^{\mathrm{p}} \geqslant 0. \tag{24}$$

In the absence of plastic evolution, i.e. $\dot{\boldsymbol{\varepsilon}}^{\mathrm{p}} = \mathbf{0}$, the dissipation must be zero, which leads to the constitutive equation for the stress:

$$\boldsymbol{\sigma} = \frac{\partial\hat{\psi}}{\partial\boldsymbol{\varepsilon}^{\mathrm{e}}}. \tag{25}$$

Moreover, when plastic evolution occurs, the rate of dissipation must be positive:

$$\varphi = \boldsymbol{\sigma} \cdot \dot{\boldsymbol{\varepsilon}}^{\mathrm{p}} \geqslant 0, \tag{26}$$

which imposes an important thermodynamic restriction on the flow rule that prescribes the plastic rate-of-deformation $\dot{\boldsymbol{\varepsilon}}^{\mathrm{p}}$.

2.4. Hyperelasticity

We assume a quadratic form of the free Helmholtz energy:

$$\hat{\psi} = \frac{1}{2}\boldsymbol{\varepsilon}^{\mathrm{e}} \cdot \mathscr{C}\boldsymbol{\varepsilon}^{\mathrm{e}} \tag{27}$$

and thus according to Eq. (25)

$$\boldsymbol{\sigma} = \mathscr{C}\boldsymbol{\varepsilon}^{\mathrm{e}} \tag{28}$$

while the second-order elasticity tensor $\mathscr{C}$ denotes the diagonal matrix of the elastic moduli:

$$\mathscr{C} = \begin{bmatrix} G_{TW} & 0 & 0 \\ 0 & G_{TL} & 0 \\ 0 & 0 & E_{TT} \end{bmatrix}. \tag{29}$$

The elastic moduli can be found from micromechanical analysis (Kelsey et al., 1958; Grediac, 1993; Gibson and Ashby, 1997). The underlying assumption is that, even for large deformations, the material remains orthotropic and the elastic moduli stay constant. The simple elasticity model adopted here is considered predominantly for numerical purpose. A more detailed description requires further research on the evolution of the elastic properties under large plastic deformation.

2.5. Yield surface

Results from biaxial experiments on metallic honeycomb in the T–W plane (Fig. 3) are typically represented by two characteristic envelopes in τ_{TW}–σ_{TT} space: (1) the initial collapse envelope and (2) the crushing envelope (Mohr and Doyoyo, 2004a,b). Both envelopes represent the behavior under out-of-plane compression and shear, a loading condition that is the focus of the present work. The collapse envelope describes the initial peak stress observed in the stress–strain curves under combined compression and shear. It determines the elastic domain for the initial, undeformed honeycomb microstructure that is free from any plastic loading history. Once plastic deformation occurs in the honeycomb under compression, the initial collapse envelope may not be recovered. In other words, the collapse envelope is important for problems dealing with the onset of plastic deformation such as the damage evaluation of sandwich components after accidental loading. In the case of large plastic deformation, the crushing envelope is of greater importance. The stress–strain curves exhibit long plateau regimes where the stresses fluctuate around their so-called plateau values. In the T–W plane, the relationship between the shear and normal plateau stresses is described by the crushing envelope:

$$\frac{\sigma_{TT}}{s^0_{TT}} + \left|\frac{\tau_{TW}}{s^0_{TW}}\right|^{\mathrm{m}} = 1, \tag{30}$$

where s^0_{TT} and s^0_{TW} denote the plateau stresses under uniaxial compression and pure shear loading, respectively. Here, we extend this experimentally observed concept of a crushing envelope to the three-dimensional case and suggest the following yield surface to describe the boundary of the elastic domain under large out-of-plane deformation:

$$f(\boldsymbol{\sigma}, \mathbf{s}) = \frac{\sigma_{TT}}{s_{TT}} + \left[\left(\frac{\tau_{TW}}{s_{TW}}\right)^2 + \left(\frac{\tau_{TL}}{s_{TL}}\right)^2\right]^{m/2} - 1 = 0. \tag{31}$$

The vector $\mathbf{s}^{\mathrm{T}} = \{s_{TW}, s_{TL}, s_{TT}\}$ denotes the deformation resistance. It is constant in the crushing regime, but increases in the densification regime as described later. Note that for $\tau_{TL} = 0$ we recover the crushing envelope in the T–W plane. The elliptic interaction in the shear plane was chosen such that the yield surface represents a transversely isotropic material for the special case $s_{TL} = s_{TW}$.

2.6. Flow rule

Denoting the direction of plastic flow by the unit vector $\mathbf{r} = \mathbf{r}(\boldsymbol{\sigma})$, the flow rule reads

$$\mathrm{d}\boldsymbol{\varepsilon}^{\mathrm{p}} = \mathrm{d}\lambda \mathbf{r}, \tag{32}$$

where the plastic multiplier $\mathrm{d}\lambda$ obeys the loading/unloading conditions:

$$\mathrm{d}\lambda \geqslant 0 \quad \text{and} \quad f\,\mathrm{d}\lambda = 0. \tag{33}$$

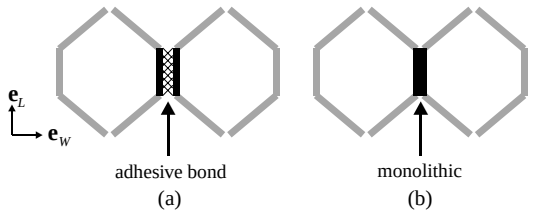

Fig. 7. (a) The adhesive bond in the 'real honeycomb' has finite strength, while (b) the bond in the 'virtual honeycomb' has infinite strength, i.e. it is modeled as monolithic.

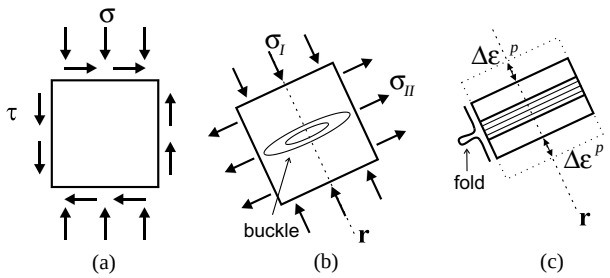

Fig. 8. Single plate under combined compression and shear: (a) stress state in terms of shear and normal stress, (b) corresponding principal stress state, (c) post-buckling response.

Virtual experiments [1] on a monolithic [2] metallic honeycomb revealed that plastic flow in a honeycomb under compression and shear in the T–W plane is approximately coaxial with the direction of the compressive principal stress (Mohr and Doyoyo, 2004b), Fig. 7. Recall that the honeycomb microstructure is composed of thin plates. When combinations of shear and normal stresses are applied to a single thin plate, buckles form perpendicular to the compressive principal stress (Fig. 8b). Under large deformations, these buckles transform into deeper folds. In order to minimize membrane stretching, the plate shortens macroscopically as the material 'flows into the fold' (Fig. 8c). This simple mechanism suggests an explanation as to why the direction of plastic flow in a monolithic honeycomb is fairly close to the direction of the macroscopic compressive principal stress.

To incorporate this phenomenological flow rule in our present model, we calculate the direction of the principal stress based on the stress vector $\boldsymbol{\sigma}$. The direction of the principal stress is found from the spectral decomposition of the corresponding stress tensor into its eigenvalues σ_{I}, σ_{II}, σ_{III} and its eigenvectors $\mathbf{t}^{\mathrm{I}}$, $\mathbf{t}^{\mathrm{II}}$, $\mathbf{t}^{\mathrm{III}}$:

$$\begin{aligned}&\tau_{TW}(\mathbf{e}_1\otimes\mathbf{e}_3+\mathbf{e}_3\otimes\mathbf{e}_1)+\tau_{TL}(\mathbf{e}_2\otimes\mathbf{e}_3+\mathbf{e}_3\otimes\mathbf{e}_2)+\sigma_{TT}(\mathbf{e}_3\otimes\mathbf{e}_3)\\&\quad=\sigma_{\mathrm{I}}\mathbf{t}^{\mathrm{I}}\otimes\mathbf{t}^{\mathrm{I}}+\sigma_{\mathrm{II}}\mathbf{t}^{\mathrm{II}}\otimes\mathbf{t}^{\mathrm{II}}+\sigma_{\mathrm{III}}\mathbf{t}^{\mathrm{III}}\otimes\mathbf{t}^{\mathrm{III}}.\end{aligned}\tag{34}$$

[1] In virtual experiments, the cell walls of a honeycomb are discretized with very fine shell meshes; subsequently, macroscopic response of the virtual honeycomb is determined from non-linear finite elements simulations under various loading conditions. Using this approach, Mohr and Doyoyo (2004b) studied the plasticity of aluminum honeycomb under combined normal and shear loading.

[2] Fig. 7 illustrates the differentiation between a 'monolithic honeycomb' and a 'real honeycomb'. In a real honeycomb, neighboring cell walls are adhesively bonded to each other, which allows for additional microstructural deformation mechanisms related to intercellular delamination. In virtual experiments, it is possible to investigate a monolithic honeycomb, which has an infinitely strong bond.

After ordering the eigenvalues such that $\sigma_{\mathrm{I}} \leqslant \sigma_{\mathrm{II}} \leqslant \sigma_{\mathrm{III}}$, the direction of plastic flow in a monolithic honeycomb is given by the eigenvector $\mathbf{t}^{\mathrm{I}} = \mathbf{t}^{\mathrm{I}}(\boldsymbol{\sigma})$ corresponding to the smallest eigenvalue:

$$\mathbf{r} = -\mathrm{sign}(t_3^{\mathrm{I}})\mathbf{t}^{\mathrm{I}}(\boldsymbol{\sigma}). \tag{35}$$

The sign correction guarantees that the vector **r** points away from the yield surface. Fig. 9 compares the direction of plastic flow according to Eq. (35) with the experimental results and the normality flow rule. It can be seen from Fig. 9 that the direction of plastic flow according to the normality rule does not correspond to the experimentally determined direction of plastic flow. However, the assumption of plastic flow in the direction of the minimum principal stress yields satisfactory results for the behavior of the monolithic honeycomb. In a real honeycomb, the microstructural deformation mechanisms are perturbed by the intercellular delamination between neighboring cell walls as well as local cell wall fracture (Fig. 10). Such microstructural effects change the driving stress state in the cell walls. More specifically, delamination-induced discontinuities in the shear stress field generate normal stresses along the T-direction (Fig. 11). In our model, this effect is taken into account by introducing the flow rule parameter $\Delta\sigma$ into the flow rule. It

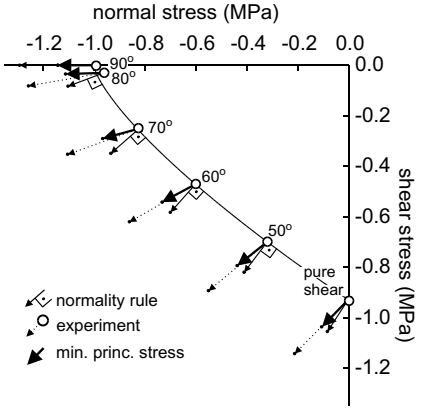

Fig. 9. Direction of plastic flow at various points on the yield surface in aluminum honeycomb (virtual experiments, label next to each data point denotes the biaxial loading angle α as defined in Fig. 13). The dashed vectors show the experimentally measured direction $\mathrm{d}\boldsymbol{\varepsilon}^{\mathrm{p}}$, the thin solid vectors represent the prediction according to normality flow rule, while the thick solid vectors indicate the direction of the minimum principal stress $\mathbf{t}^{\mathrm{I}}$.

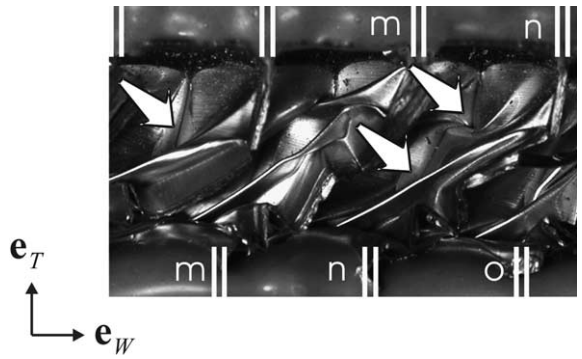

Fig. 10. Side view of a deformed honeycomb specimen. The bold arrows point at the locations of partial delamination between neighboring cell walls.

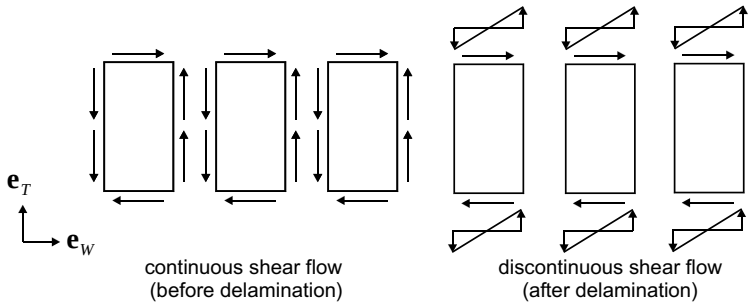

Fig. 11. Shear flow in a honeycomb.

allows for the adjustment of the direction of plastic flow. Instead of using the stress state described by the stress vector $\boldsymbol{\sigma}$, we use the perturbed stress vector $\boldsymbol{\sigma} + \Delta\sigma\mathbf{e}_3$ as a basis for the calculation of the direction of plastic flow. Formally, we rewrite Eq. (35) as

$$\mathbf{r}(\boldsymbol{\sigma}) = -\mathrm{sign}(t_3^{\mathrm{I}})\mathbf{t}^{\mathrm{I}}(\boldsymbol{\sigma} + \Delta\sigma\mathbf{e}_3). \tag{36}$$

The calibration of the flow rule parameter $\Delta\sigma$ is discussed in Section 3.1. Regarding thermodynamics, it must be noted that the present combination of flow rule and yield surface fulfills the non-negativity requirement of the intrinsic dissipation. However, the model may not be applied without restriction in loading situations involving tensile stresses ($\sigma_{TT} > 0$). Firstly, the mechanisms change under tension along the T-direction (Doyoyo and Mohr, 2003) and consequently both the yield surfaces as well as the flow rule no longer apply. Secondly, as the plastic strain rate along the T-direction is always negative according to our flow rule ($\mathrm{d}\varepsilon_{TT}^{\mathrm{p}} \leqslant 0$), the product of normal stress and normal strain rate is negative for tension ($\mathrm{d}\varepsilon_{TT}^{\mathrm{p}}\sigma_{TT} \leqslant 0$). Thus, depending on the shear dissipation, the total plastic dissipation might become negative which would violate the non-negativity requirement of the intrinsic dissipation (Eq. (26)).

2.7. Strain hardening—densification

The deformation resistance remains constant throughout the crushing regime where the components of the deformation resistance vector correspond to the plateau stresses, $\mathbf{s}^0 = \{s_{TW}^0, s_{TL}^0, s_{TT}^0\}^{\mathrm{T}}$. Significant strain hardening is a characteristic of the densification regime as cell wall contact within the microstructure continually raises the load carrying capacity of the honeycomb. We extend the results from uniaxial experiments (Mohr and Doyoyo, 2003b) to the multiaxial case by relating strain hardening to plastic strain along the T-direction, $\varepsilon_{TT}^{\mathrm{p}}$, and by assuming a geometrically self-similar evolution of the yield surface. The evolution equation for the deformation resistance vector $\mathbf{s}$ reads

$$\mathrm{d}\mathbf{s} = \mathrm{d}\lambda\mathbf{q}, \tag{37}$$

where we have the initial condition

$$\mathbf{s}(\varepsilon_{TT}^{\mathrm{p}} = 0) = \mathbf{s}^0 \tag{38}$$

and

$$\left.\begin{array}{ll} \mathbf{q} = \mathbf{0} & \text{for } \varepsilon_{TT}^{\mathrm{p}} \geqslant \varepsilon_{\mathrm{d}} \\ \mathbf{q} = \dfrac{h_{\mathrm{d}}}{1+\varepsilon_{TT}^{\mathrm{p}}}\dfrac{r_3}{s_{TT}^0}\mathbf{s}^0 & \text{for } \varepsilon_{TT}^{\mathrm{p}} < \varepsilon_{\mathrm{d}} \end{array}\right\}. \tag{39}$$

h_{d} is the densification modulus and ε_{d} is the densification strain. The factor $h_{\mathrm{d}}/(1+\varepsilon_{TT}^{\mathrm{p}})$ is introduced based on the results from uniaxial experiments (Mohr and Doyoyo, 2003b).

2.8. Consistency condition

We write the consistency condition formally as

$$\mathrm{d}f = 0. \tag{40}$$

The consistency condition allows for the determination of the plastic multiplier $\mathrm{d}\lambda$.

2.9. Objectivity

A change of observer does not affect the present formulation as all equations are given in material coordinates. Thus, we limit our attention to the verification of objectivity under rigid body rotations. Under a rigid body rotation $\mathbf{Q}$, the deformation gradient transforms as

$$\mathbf{F} \to \mathbf{QF}. \tag{41}$$

According to the decomposition of the deformation gradient defined in Eq. (5), we have

$$\mathbf{R} \to \mathbf{QR}, \tag{42}$$

$$\mathbf{U} \to \mathbf{U}, \tag{43}$$

and hence

$$\mathbf{E} \to \mathbf{E}, \tag{44}$$

which implies that the elastic and plastic strain vectors remain invariant under rigid body rotation:

$$\boldsymbol{\varepsilon}^{\mathrm{e}} \to \boldsymbol{\varepsilon}^{\mathrm{e}}, \tag{45}$$

$$\boldsymbol{\varepsilon}^{\mathrm{p}} \to \boldsymbol{\varepsilon}^{\mathrm{p}}. \tag{46}$$

The Cauchy stress tensor transforms objectively under rigid body rotation

$$\mathbf{T} \to \mathbf{QTQ}^{\mathrm{T}} \tag{47}$$

while the stress tensor as defined in Eq. (18) remains unaltered:

$$\mathbf{T}^{*} \to (\det \mathbf{U})(\mathbf{QR})^{\mathrm{T}}\mathbf{QTQ}^{\mathrm{T}}(\mathbf{QR})\mathbf{U}^{-\mathrm{T}} = (\det \mathbf{U})\mathbf{R}^{\mathrm{T}}\mathbf{TRU}^{-\mathrm{T}} = \mathbf{T}^{*}. \tag{48}$$

It follows that the stress vector is frame-indifferent as well:

$$\boldsymbol{\sigma} \to \boldsymbol{\sigma}. \tag{49}$$

3. Application

A user-subroutine for the finite element code Abaqus/explicit (HKS, 2001) has been developed to utilize the present constitutive model in structural applications. For this, the constitutive equations have been numerically integrated using a backward Euler algorithm.

3.1. Identification of model parameters

The elastic moduli G_{TW}, G_{TL}, and E_{TT} are directly determined from the micromechanical models that are summarized in the textbook by Gibson and Ashby (1997). The plateau normal stress s^{0}_{TT}, the densification strain ε_{d}, and the hardening modulus h_{d} are conveniently found from a uniaxial compression test (Fig. 2).

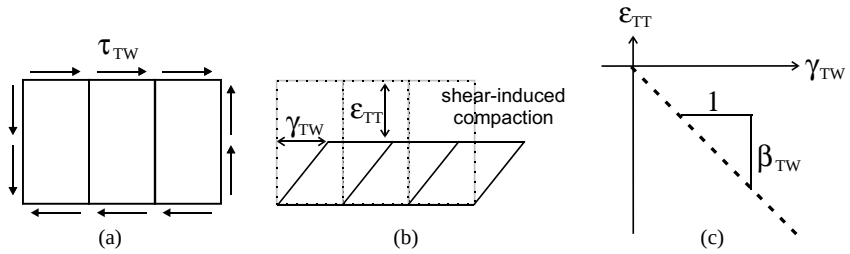

Fig. 12. Honeycomb behavior under pure shear loading: (a) stress state, note that $\sigma_{TT} = 0$, (b) deformed material, (c) measured normal vs. shear strain curve.

The shear plateau stresses s^0_{TW} and s^0_{TL} can be directly obtained from pure shear tests in the T–W and T–L planes, respectively (for experimental details, see Mohr and Doyoyo, 2003a). Either of the shear tests also allows for the calibration of the flow rule parameter $\Delta\sigma$. Note that the flow rule controls the shear compaction/dilatancy of a plastically deforming material (e.g. Anand and Gu, 2000). To describe the compaction behavior under pure shear loading in the T–W plane ($\sigma_{TT} = 0$), we introduce the compaction parameter β_{TW} that expresses the ratio of normal and shear strains:

$$\beta_{TW} := \frac{\mathrm{d}\varepsilon^{\mathrm{p}}_{TT}}{|\mathrm{d}\gamma^{\mathrm{p}}_{TW}|} = -\tan\chi, \tag{50}$$

where the angle χ is determined by the flow rule (Eq. (36)). Upon evaluation for pure shear, we find

$$\tan 2\chi = \frac{2s^0_{TW}}{\Delta\sigma}. \tag{51}$$

In what follows, for $\Delta\sigma = 0$, we have $\chi = 45°$ and thus $\beta_{TW} = -1$. In other words, the amount of shear and compressive deformation are identical under pure shear loading. For $\Delta\sigma < 0$, we increase the amount of shear-induced normal deformation, whereas for $\Delta\sigma > 0$, it is reduced.

Fig. 12 shows a schematic of a pure shear test. By measuring the shear-induced normal strain throughout a pure shear test, β_{TW} is found from the slope of the shear vs. normal strain curve (Fig. 12c). Thus, after rewriting Eqs. (50) and (51), we find the flow rule parameter $\Delta\sigma$ as

$$\Delta\sigma = \left(\beta_{TW} - \frac{1}{\beta_{TW}}\right) s^0_{TW}. \tag{52}$$

Based on the results from experiments on aluminum honeycomb, it appears that the shear exponent is generally $m = 1.4$. However, the existing experimental data on metallic honeycombs is still limited and at this stage, we recommend biaxial tests for the calibration of the shear exponent. Details on the calibration procedure for the shear exponent m, the shear plateau stresses s^0_{TW} and s^0_{TL}, and the flow rule parameter $\Delta\sigma$ based on biaxial tests are given in Appendix A.

It shall be noted that we could also use the results from a shear test in the T–L plane to determine the flow rule parameter. However, as the extent of delamination under loading in the T–L plane may differ from that under loading in the T–W plane, the flow rule parameter $\Delta\sigma$ may depend on the direction of transverse shear, that is $\Delta\sigma = \Delta\sigma(\mathrm{d}\gamma_{TL}/\mathrm{d}\gamma_{TW})$.

3.2. Uniaxial compression

We simulate the uniaxial compression experiments on hexagonal aluminum 5056-H39 honeycomb, where block specimens (195×195×200 mm) have been subjected to quasi-static loading along the

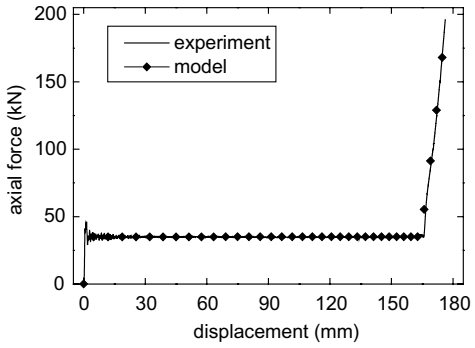

Fig. 13. Axial force (compression) vs. displacement in a uniaxial compression experiment of honeycomb specimens.

Table 2
Material properties and model parameters of 1.8% relative density hexagonal aluminum 5056-H39 honeycomb

Experiment type	S^0_{TW} (MPa)	s^0_{TT} (MPa)	m (–)	ε_d (–)	h_d (MPa)	$\Delta\sigma$ (MPa)
Uniaxial (physical)	–	−0.93	–	0.82	10.7	–
Combined (virtual)	0.93	−1.0	1.35	0.82	10.7	0.08
Combined (physical)	0.51	−0.93	1.40	0.82	10.7	0.30

T-direction (Mohr and Doyoyo, 2003b). The honeycomb had a cell size $D = 4.75$ mm, a single cell wall thickness $t = 33$ μm, and 1.8% relative density. Fig. 13 shows the force–displacement curves for the experiment and for the numerical simulation with the model parameters $s^0_{TT} = 0.92$ MPa, $\varepsilon_d = 0.82$ and $h_d = 10.2$ MPa (Table 2). The part of the model to be verified by this simulation is the evolution law for the deformation resistance (Eq. (39)). The good correlation between the experimental and numerical results in the densification regime supports the choice of the densification law.

3.3. Combined compression and shear

Here, we simulate experiments where the honeycomb is loaded along a linear strain path in the T–W plane and the corresponding stress states in the crushing regime are combined compression and shear ($\sigma_{TT} \leqslant 0$). The schematic in Fig. 14 illustrates this loading condition. It is characterized by the biaxial loading angle α, which is kept constant throughout each test. We use two sets of experimental data for the validation of the constitutive model.

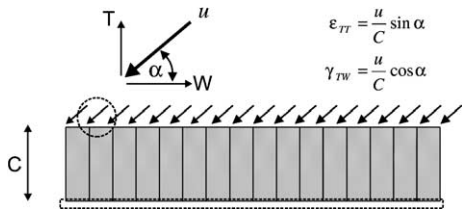

Fig. 14. A schematic of a biaxial test set-up on a honeycomb core.

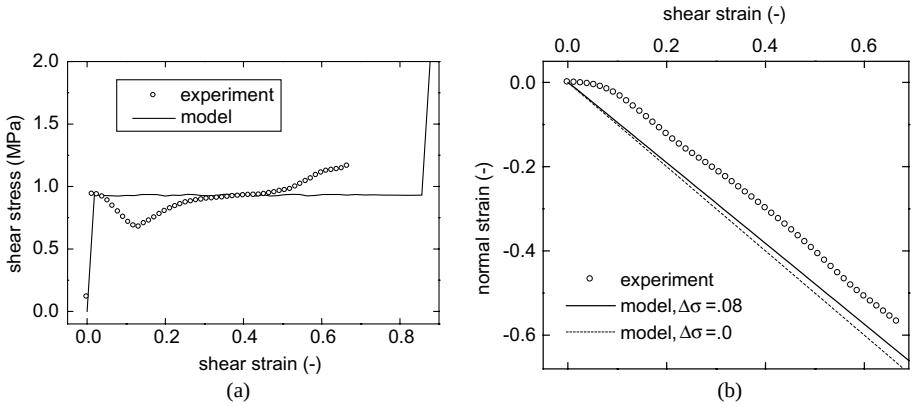

Fig. 15. Simulation of the virtual experiments on aluminum honeycomb for pure shear loading ($\sigma_{TT} = 0$): (a) shear stress vs. shear strain, (b) normal strain vs. shear strain.

3.3.1. Virtual experiments

Recall that virtual experiments characterize the mechanical behavior of a monolithic honeycomb (Mohr and Doyoyo, 2004b). The uniaxial crushing plateau stress as determined from a virtual crush test was $s^0_{TT} = -1.0$ MPa. Fig. 15a shows the macroscopic stress–strain curve of the corresponding virtual pure shear test. The mean stress is the shear plateau stress $s^0_{TW} = 0.93$ MPa. As shown in Fig. 9 and discussed above, the assumption of plastic flow in the direction of the minimum principal stress provides a good approximation for the monolithic honeycomb. However, though introduced to account for delamination in real honeycombs, we may use the flow rule parameter to fit the model to the experimental data (this can only be done for one test). For instance, the shear-induced compaction in the virtual pure shear test is $\beta_{TW} = -0.96$. Upon evaluation of Eq. (52), we find a flow rule parameter of $\Delta\sigma = 0.08$ MPa, which provides a slightly better prediction of the shear-induced compaction than the mechanism-based choice of $\Delta\sigma = 0$ (Fig. 15b).

Regarding pure shear, the constitutive model assumes a constant shear dilatancy ratio; this assumption agrees well with the experiment at large shear strains, but cannot capture the initial non-linearity in the experimental shear vs. normal strain curve (Fig. 15b). For large loading angles, we compare the stress–strain curves as obtained from virtual experiments with the model predictions (Fig. 16a–h). The initial peaks observed in experiments are not seen in the model curves as they are not part of the constitutive formulation. Experiments and simulations agree well in the crushing regime; the mean stress level that is determined by the interaction of yield surface and flow rule is successfully represented. The results are poor for loading angles where the concept of plateau stresses does not fully apply. For instance, observe that the shear response under 80° loading shows significant fluctuations with respect to its mean value.

3.3.2. Physical experiments

In this test series, the same aluminum honeycomb that was tested in the uniaxial experiments has been subjected to various combinations of normal and shear loading (Mohr and Doyoyo, 2004a). The model parameters have been identified using the model calibration procedure for biaxial tests as outlined in Appendix A. A good fit of the yield envelope given by Eq. (31) to the experimental data points is found for $s^0_{TT} = -0.92$ MPa, $s^0_{TW} = 0.51$ MPa and $m = 1.40$. Best overall fit of the flow rule is found for $\Delta\sigma = 0.3$ MPa (Fig. 18), which corresponds to a shear-induced compaction of $\beta_{TW} = -0.75$.

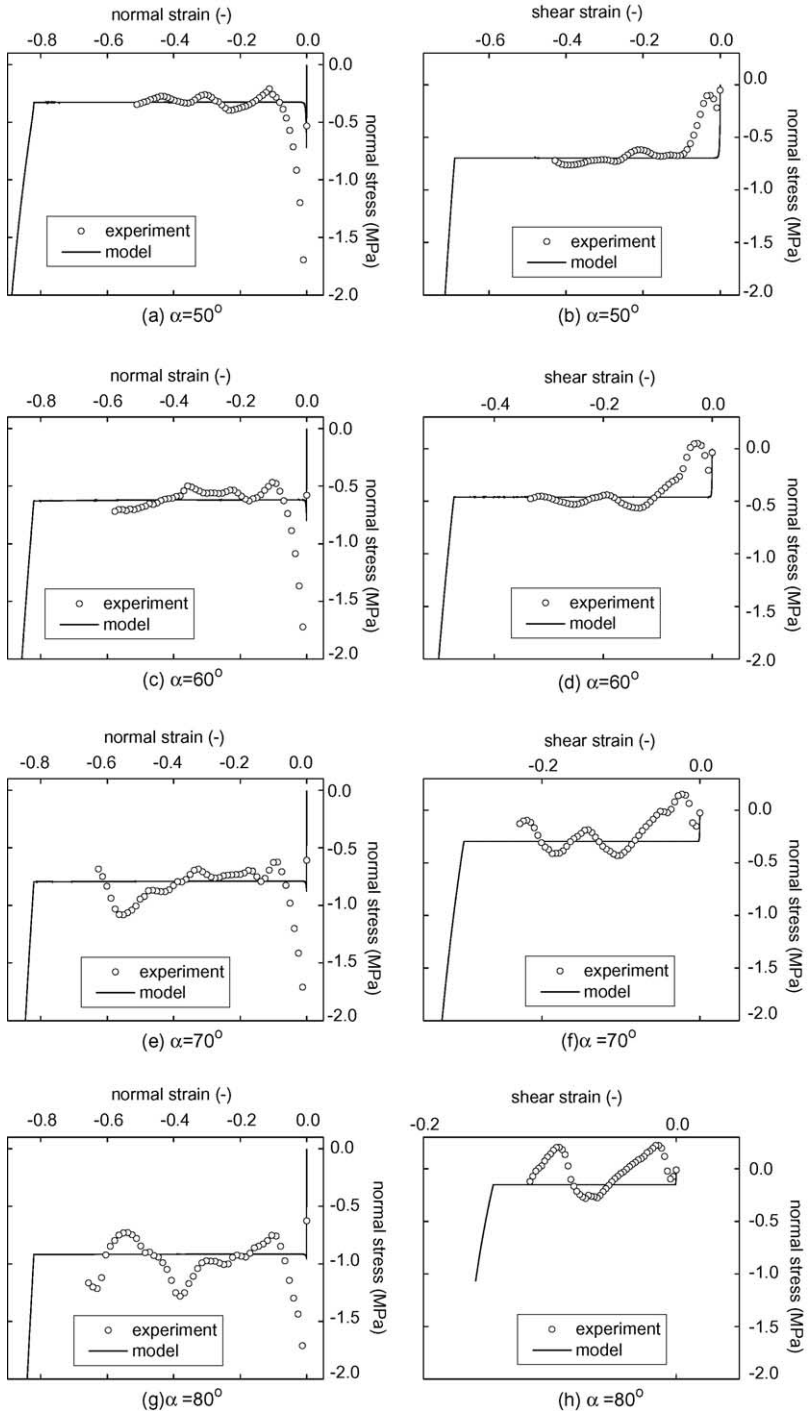

Fig. 16. Simulation of the virtual experiments on aluminum honeycomb under combined loading.

Fig. 17 demonstrates the excellent agreement of the experimental results with model predictions. As compared to the stress–strain curves for the virtual honeycomb, the fluctuation in the response curves of the

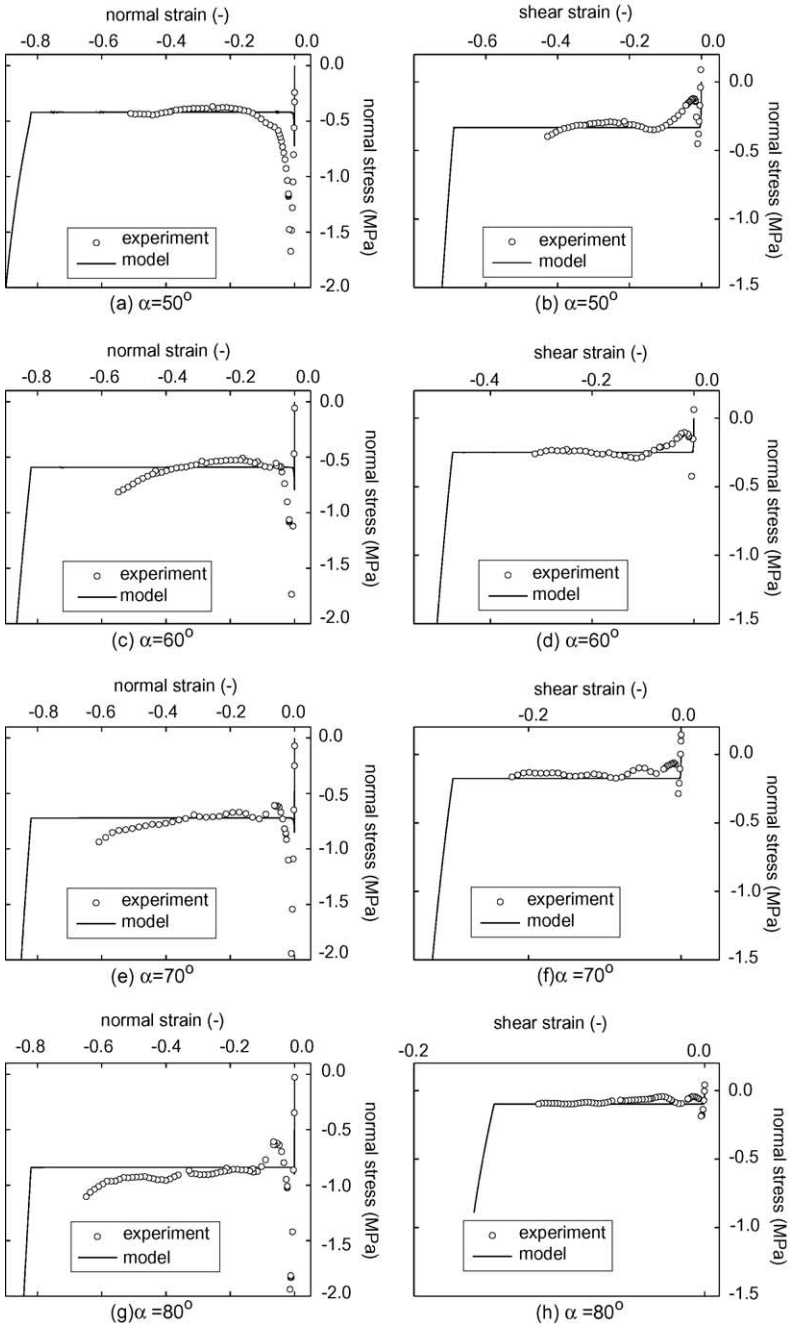

Fig. 17. Simulation of the physical experiments on aluminum honeycomb under combined loading.

physical experiments are smaller and thus, the concept of plateau stresses yields a good approximation for all loading angles.

3.4. Limitations

The generic term 'metallic honeycomb' stands for a large family of cellular materials with two-dimensional periodic microstructures. One example is the hexagonal thin-walled aluminum honeycomb that was investigated here. The backbone of the present constitutive model is the concept of plateau stresses. Throughout the empirical development of the phenomenological constitutive model, we used the results from the virtual and physical quasi-static biaxial experiments on aluminum honeycomb. The universal potential of the present model must be shown in the future. However, there are various known and anticipated limitations of the present model that are noteworthy:

- *Tension.* The model does not provide reliable predictions when tensile stresses are applied along the T-direction. Experiments have shown that the constitutive response under tension is dramatically different from that under compression (Doyoyo and Mohr, 2003). For simplicity, we did not include the tensile behavior. Moreover, most practical applications do not include tension as it is rather rare that out-of-plane tensile loads are applied to a honeycomb.
- *Fracture.* For example, honeycomb fracture is frequently observed in impact barriers that are used for passenger car crash tests. As compared to other engineering materials, fracture of honeycomb requires special treatment in terms of modeling. In particular, the influence of large in-plane deformation is expected to come into play.
- *Strain rate effects.* Strain rate effects on the macroscopic level are expected at high loading velocities where the lateral inertia of the folding cell walls influences the fold mechanics of the microstructure. The applicability of the concept of plateau stresses must be carefully examined for high loading velocities.
- *Deformation-induced anisotropy and evolving elastic moduli.* Recall the assumptions made on the elastic part of the constitutive equations. Metallic honeycomb becomes fully anisotropic under large deformations, which goes along with a change of its elastic moduli (Mohr and Doyoyo, 2003b). Thus, the simple hyperelastic law adopted here does not allow for an analysis of wave propagation or other phenomena that require an accurate description of the variation of the elastic strain energy.

4. Conclusion

A finite-strain orthotropic rate-independent constitutive model for thin-walled metallic honeycomb has been developed. The foundation of the model is the experimental observation of plateau stresses in the crushing regime of the honeycomb under large deformation. The constitutive model comprises a conical yield surface in the shear vs. normal stress space along with a non-associated flow rule. The model has been incorporated into a finite element code and has been successfully employed to predict the mechanical response of physical and virtual honeycomb specimens under various biaxial loading conditions in the T–W plane. The limitations of the model have also been discussed in detail. From an engineering design point of view, reliable prediction of the response in the T–W plane may be satisfactory as it provides an 'acceptable lower bound' for the amount of energy absorbed in honeycomb cores in sandwich structures. However, testing and validation in the T–L plane is recommended for honeycombs with pronounced orthotropic in-plane properties.

Acknowledgements

We thank Professor Tomasz Wierzbicki for various discussions. The authors are grateful to Professor Lallit Anand for his valuable comments and providing a well-documented example user material subroutine for ABAQUS/explicit. Financial support by the Joint MIT/Industry Ultralight Consortium and the Cambridge-MIT Institute (CMI) is acknowledged.

Appendix A. Model calibration based on biaxial tests

The biaxial test set-up that is described in the schematic of Fig. 14 has proven to be a reliable testing technique to determine the mechanical behavior of a honeycomb (Mohr and Doyoyo, 2003a, 2004a,b; Doyoyo and Mohr, 2003). This set-up may also be used to calibrate the present constitutive model for a large class of honeycomb materials with various microstructural profiles. We suggest that this biaxial test set-up be used to evaluate the shear plateau stresses s^0_{TW} and s^0_{TL}, and the flow rule parameter $\Delta\sigma$ for the honeycomb as an alternative to pure shear tests. This method will also ensure the reliable determination of the shear exponent m that may vary for different types of honeycombs.

Given the plateaus stresses from biaxial tests at different loading angles (Fig. 18), the shear plateau stresses s^0_{TW} and s^0_{TL}, as well as the shear exponent m are found from fitting the mathematical expression for the yield surface (Eq. (31)) to the experimental data. The calibration of the flow rule parameter on the other hand requires further insight in the model behavior. Consider combined shear and normal loading in the T–W plane ($\boldsymbol{\sigma} = \tau_{TW}\mathbf{e}_1 + \sigma_{TT}\mathbf{e}_3$) along a linear monotonic strain path under compression ($\sigma_{TT} \leqslant 0, \mathrm{d}\lambda > 0$) in the crushing regime:

$$\mathrm{d}\boldsymbol{\varepsilon} = -\mathrm{sign}(\tau_{TW})[\cos\alpha\mathbf{e}_1 + \sin\alpha\mathbf{e}_3] \quad \text{and} \quad \gamma_{TL} = 0, \tag{A.1}$$

where $\alpha \in [0, \pi/2]$ denotes the biaxial loading angle. In the crushing regime, we have steady state conditions, characterized by

$$\left.\begin{aligned} \mathrm{d}\boldsymbol{\sigma} &= \mathbf{0} \\ \mathrm{d}\mathbf{s} &= \mathbf{0} \end{aligned}\right\}. \tag{A.2}$$

It follows from the elastic constitutive equation (Eq. (28)) that $\mathrm{d}\boldsymbol{\sigma} = \mathscr{C}(\mathrm{d}\boldsymbol{\varepsilon} - \mathrm{d}\boldsymbol{\varepsilon}^{\mathrm{p}})$ and hence $\mathrm{d}\boldsymbol{\varepsilon} = \mathrm{d}\boldsymbol{\varepsilon}^{\mathrm{p}}$. Thus, the stress state $\boldsymbol{\sigma}$ is determined by the following equations:

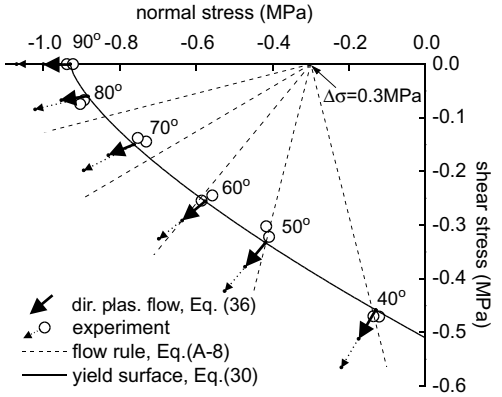

Fig. 18. Model calibration for the physical experiments on aluminum honeycomb.

$$f(\boldsymbol{\sigma}) = 0, \tag{A.3}$$

$$\mathbf{r}(\boldsymbol{\sigma}) = \frac{\mathrm{d}\boldsymbol{\varepsilon}^{\mathrm{p}}}{\mathrm{d}\lambda} = \frac{\mathrm{d}\boldsymbol{\varepsilon}}{\mathrm{d}\lambda}. \tag{A.4}$$

In other words, under steady state conditions, the solution $\boldsymbol{\sigma}$ is the point on the yield surface for which the direction of plastic flow $\mathbf{r}(\boldsymbol{\sigma})$ coincides with the direction of the applied total strain increment $\mathrm{d}\boldsymbol{\varepsilon}$. Mathematically, we may express this requirement of coaxiality as

$$\tan\chi = \tan\alpha, \tag{A.5}$$

where we introduced χ as the angle between the W-axis and the direction of flow, that is

$$\mathbf{r} = \operatorname{sign}(\tau_{TW})\cos\chi\mathbf{e}_1 - \sin\chi\mathbf{e}_3. \tag{A.6}$$

The angle χ is obtained from the spectral composition defined in Eq. (34). Upon evaluation, we have

$$0 \leqslant \chi < \pi/2: \quad \tan 2\chi = \frac{2|\tau_{TW}|}{\sigma_{TT} + \Delta\sigma}. \tag{A.7}$$

It follows from Eqs. (A.5) and (A.7) that the direction of plastic flow coincides with the loading direction α^*, for all stress states (σ_{TT}, τ_{TW}) that lie on the line

$$|\tau_{TW}| = \frac{1}{2}(\sigma_{TT} + \Delta\sigma)\tan 2\alpha^*. \tag{A.8}$$

We make use of Eq. (A.8) to calibrate the flow rule parameter. After fitting the yield surface to the experimental data points, we can assume that Eq. (A.3) is satisfied for any experimental point $(\sigma^*_{TT}, \tau^*_{TW})$. Furthermore, Eq. (A.8) must be satisfied, which allows us to determine the flow rule parameter:

$$\Delta\sigma = \frac{2|\tau^*_{TW}|}{\tan 2\alpha^*} - \sigma^*_{TT}. \tag{A.9}$$

For example, consider the experimental data point ($\sigma^*_{TT} = -0.14$ MPa, $\tau^*_{TW} = -0.47$ MPa) for a biaxial test at a fixed loading angle $\alpha^* = 40°$ (Fig. 18). Upon evaluating of Eq. (A.9), we find $\Delta\sigma = 0.3$ MPa. Using $\Delta\sigma = 0.3$ MPa, we plotted Eq. (A.8) for different biaxial loading angles (see dashed lines in Fig. 18). The intersection points of the dashed lines and the yield surface correspond to the model predictions. Comparison with the adjacent experimental data points demonstrates the quality of the flow rule parameter calibration based on the result for $\alpha^* = 40°$ loading.

References

Anand, L., Gu, C., 2000. Granular materials: constitutive equations and strain localization. Journal of the Mechanics and Physics of Solids 48, 1701–1733.

Doyoyo, M., Mohr, D., 2003. Microstructural response of aluminum honeycomb to combined out-of-plane loading. Mechanics of Materials 35 (9), 865–876.

ESI, 2000. Engineering Systems International. PamCrash reference manuals.

Geymonat, G., Muller, S., Triantafyllidis, N., 1993. Homogenization of non-linearly elastic materials, microscopic bifurcation and macroscopic loss of rank-one convexity. Archives of Rational Mechanics and Analysis 122, 231–290.

Gibson, L.J., Ashby, M.F., 1997. Cellular Solids: Structure and Properties, second ed. Cambridge University Press, Cambridge.

Grediac, M., 1993. A finite element study on the transverse shear in honeycomb cores. International Journal of Solids and Structures 30, 1777–1788.

Gurtin, M.E., 1981. An Introduction to Continuum Mechanics. Academic Press, New York.

HKS 2001. ABAQUS Reference Manuals, Version 6.1, Hibbitt, Karlsson & Sorensen Inc., Pawtucket, RI.

Kelsey, S., Gellatly, R.A., Clark, B.W., 1958. The shear modulus of foil honeycomb cores. Aircraft Engineering 30, 294–302.

Malvern, L.E., 1969. Introduction to the Mechanics of a Continuous Medium. Prentice–Hall.

Mohr, D., Doyoyo, M., 2003a. A new method for the biaxial testing of cellular solids. Experimental Mechanics 43 (2), 173–182.
Mohr, D., Doyoyo, M., 2003b. Nucleation and propagation of plastic collapse bands in aluminum honeycomb. Journal of Applied Physics 94 (4), 2262–2270.
Mohr, D., Doyoyo, M., 2004a. Experimental investigation on the plasticity of Hexagonal Aluminum honeycomb under multiaxial loading. Journal of Applied Mechanics 71 (3).
Mohr, D., Doyoyo, M., 2004b. Deformation-induced folding systems in thin-walled monolithic hexagonal metallic honeycomb. International Journal of Solids and Structures, in press.
Okumura, D., Ohno, N., Noguchi, H., 2002. Post-buckling analysis of elastic honeycombs subject to in-plane biaxial compression. International Journal of Solids and Structures 39, 3487–3503.
Ohno, N., Okumura, D., Noguchi, H., 2002. Microscopic symmetric bifurcation conditions of cellular solids based on a homogenization theory of finite deformation. Journal of the Mechanics and Physics of Solids 50, 1125–1153.
Schreyer, H.L., Zuo, Q.H., Maji, A.K., 1994. Anisotropic plasticity model for foams and honeycombs. Journal of Engineering Mechanics 120 (9), 1913–1930.
Triantafyllidis, N., Maker, B.N., 1985. On the comparison between microscopic and macroscopic instability mechanisms in a class of fiber-reinforced composites. ASME Journal of Applied Mechanics 52, 794–800.